

Accepted by the ApJ

Inner Structure of Protostellar Collapse Candidate B335 Derived from Millimeter-Wave Interferometry¹

Daniel W.A. Harvey, David J. Wilner, Philip C. Myers

dharvey, dwilner, pmyers@cfa.harvard.edu

Harvard-Smithsonian Center for Astrophysics, 60 Garden Street, Cambridge, MA 02138

Mario Tafalla

tafalla@oan.es

Observatorio Astronomico Nacional, Apartado 1143, E-28800 Alcala de Henares, Spain

and

Diego Mardones

mardones@das.uchile.cl

Departamento de Astronomia, Universidad de Chile, Casilla 36-D, Santiago, Chile

ABSTRACT

We present a study of the density structure of the protostellar collapse candidate B335 using continuum observations from the IRAM Plateau de Bure Interferometer made at wavelengths of 1.2 mm and 3.0 mm. We analyze these data, which probe spatial scales from 5000 AU to 500 AU, directly in the visibility domain by comparison to synthetic observations constructed from models that assume different physical conditions. This approach allows for much more stringent constraints to be derived from the data than from analysis of images. A single radial power law in density provides a good description of the data, with best fit power law density index $p = 1.65 \pm 0.05$. Through simulations, we quantify the sensitivity of this result to various model uncertainties, including assumptions of temperature distribution, outer boundary, dust opacity spectral index, and an unresolved central component. The largest uncertainty comes from the unknown presence of a centralized point source. The maximal point source

with 1.2 mm flux of $F = 12 \pm 7$ mJy reduces the power law density index to $p = 1.47 \pm 0.07$. The remaining sources of systematic uncertainty, of which the most important is the radial dependence of the temperature distribution, likely contribute a total uncertainty at the level of $\delta p \lesssim 0.2$. Taking account the uncertainties, we find strong evidence that the power law index of the density distribution within 5000 AU is significantly less than the value at larger radii, close to 2.0 from previous studies of dust emission and extinction. Images made from the data show clear departures from spherical symmetry, with the globule being slightly extended perpendicular to the outflow axis. The inclusion of a crude model of the outflow as a hollowed bipolar cone of constant opening angle improves the fit and leaves the resulting density power law index unchanged. These results conform well to the generic paradigm of isolated, low-mass star formation which predicts a power law density index close to $p = 1.5$ for an inner region of gravitational free fall onto the protostar. However, the standard inside-out collapse model does not fit the data as successfully as a simple $p = 1.5$ power law because of the relative shallowness of the predicted density profile just within the infall radius.

Subject headings: ISM: globules — ISM: individual(B335) — radio continuum: ISM — ISM: jets and outflows — stars: formation

1. Introduction

The dense core in the B335 dark globule is generally recognized as the best protostellar collapse candidate. This dense core is nearby (250 pc, Tomita, Saito & Ohtani 1979), isolated, and nearly spherical. It contains a deeply embedded low luminosity young stellar object ($3 L_\odot$) discovered at far-infrared wavelengths by Keene et al. (1983) and detected by IRAS only at $\lambda \geq 60 \mu\text{m}$. Detailed radiative transfer models based on the theory of inside-out collapse (Shu 1977) provide very good fits to spectral line profiles of the dense gas tracers CS and H₂CO observed at 10''–30'' resolution (Zhou et al. 1993; Choi et al. 1995).

Recent studies have raised serious doubts about the inside-out collapse interpretation of the molecular line profiles. Observations of the CS(5-4) line at higher angular resolution, about 500 AU, show that the high velocity emission arises from the inner part of a bipolar

¹Based on observations carried out with the IRAM Plateau de Bure Interferometer. IRAM is supported by INSU/CNRS (France), MPG (Germany) and IGN (Spain).

outflow, not from the gravitational acceleration of dense gas close to the protostar (Wilner et al. 2000). In addition, studies of starless cores show that some molecular species, in particular CS, are frozen out onto grains at densities characteristic of the inner regions of B335 (Caselli et al. 2002, Tafalla et al. 2002). If protostellar heating does not promptly desorb CS molecules from icy grain mantles, then this species likely makes a poor probe of the gas kinematics in the presumed infall zone.

Since the density field is strongly coupled to the velocity field, observations of dust emission and absorption provide an alternative means to infer the dynamical state of the dense core. Harvey et al. (2001) describe deep near-infrared extinction measurements toward B335 that show a density profile consistent with the inside-out collapse theory, in particular an r^{-2} density profile for the outer envelope and an inner turnover towards free-fall. The best fit model has an infall radius of 6500 AU (26''), similar to that derived from molecular line studies (Zhou et al. 1993; Choi et al. 1995). The extinction data also show the dramatic effect of the bipolar outflow driven by the protostar. However, extinction measurements could not be made interior to 3500 AU (14''), where no background stars are visible, even with NICMOS on HST. As a result, the extinction data could not distinguish the inside-out collapse model from, e.g. a highly unstable Bonnor-Ebert sphere, whose density profiles depart significantly from each other only at radii $\lesssim 2500$ AU.

Observations of long wavelength dust emission provide another method for probing density structure. This technique is nearly as direct as observations of dust extinction. The intensity of the emission provides an integral along the line-of-sight of the product of the density, temperature, and opacity of the dust. By modeling the dust temperature and specific mass opacity, the observed intensities may be used to constrain the density distribution. The analysis of dust emission complements extinction work because the dust emission method becomes most effective in the high column density inner regions of dense cores where dust extinction becomes large and difficult to penetrate.

Dust emission has been used very successfully to measure density structure of dense cores using bolometer cameras at millimeter and submillimeter wavelengths on large single dish telescopes, including the IRAM 30 meter (Ward-Thompson, Motte & Andre 1999, Motte & Andre 2001) and the JCMT (Ward-Thompson et al. 1994; Visser, Richer & Chandler 2001, Shirley et al. 2000). Unfortunately, the central regions of the nearest protostellar cores are generally comparable in size to the beamwidths of these telescopes and are poorly resolved. The density structure at smaller scales can only be probed with interferometers. With interferometer observations, the density structure may be strongly constrained through analysis of dust emission directly in the visibility domain. So far, detailed modeling of millimeter continuum visibility data in this context has been rarely applied (Keene & Masson

1990, Hogerheijde et al. 1999, Mundy, Looney & Welch 2000)

B335 has been imaged with millimeter interferometers in several previous studies (Chandler & Sargent 1993, Hirano et al. 1992, Saito et al. 1999). In this paper, we present observations of dust continuum emission from B335 at both 3 mm and 1.2 mm obtained with the IRAM Plateau de Bure Interferometer (PdBI) that obtain considerably better sensitivity. These observations sample well the density profile of B335 from size scales of ~ 5000 AU to ~ 500 AU, affording an order of magnitude better resolution than has been possible with single dish telescopes. The visibilities can discriminate the behaviour of the various physical models that all match the near infrared extinction in the outer regions of B335.

2. Observations

Continuum emission from B335 was observed with the IRAM PdBI simultaneously with the CS(5-4) line emission reported by Wilner et al. (2000). In brief, a single pointing was observed using 5 antennas in the D configuration giving baseline lengths from the shadowing limit of 15 meters to nearly 80 meters. The tuning was single (lower) sideband at 100 GHz (3.0 mm) and double sideband at 245 GHz (1.2 mm). The half power field of view is 50" at 3.0 mm and 20" at 1.2 mm. The absolute flux scale was determined through observations of the standard source MWC349, assumed to be 1.09 Jy at 3.0 mm at 1.82 Jy at 1.2 mm, with estimated uncertainties of 20% and 10%, respectively. Continuum visibility records at the two wavelengths were formed for each 60 second integration of the digital correlator (3×160 MHz at 1.2 mm, 1×160 MHz at 3.0 mm), excluding a few channels contaminated by molecular line emission, which resulted in 2372 records at 3.0 mm and 4824 records at 1.2 mm (after flagging occasional bad records). In addition to amplitude and phase, each record also contains a variance measure, determined from the system temperatures and antenna gains.

3. Constructing Model Visibilities

We analyze the dense core structure using the interferometer measurements directly, in the visibility domain, without producing images. While this approach is computationally intensive, it recognizes the limitations of standard Fourier inversion and deconvolution techniques, and allows a much more direct comparison with models than analyzing images, avoiding the problems caused by synthesized beam characteristics.

The B335 visibilities are compared to theoretical models of protostellar envelope structure by constructing synthetic visibilities, taking account of (1) the dust continuum radiative

transfer, and (2) the specifics of the observations, including the exact (u, v) sampling and primary beam attenuation. The analysis of dust emission requires more complexity than dust extinction, because the models must include assumptions about the temperature distribution and specific mass opacity in addition to the model density field. Since we cannot consider an exhaustive list of protostellar envelope models, we instead fix attention on a few widely promoted density fields, including simple power law descriptions, inside-out collapse, and the Bonnor-Ebert sphere. These models all successfully match the near-infrared extinction data in the outer regions of B335, beyond ~ 5000 AU, but they predict substantial differences in the inner regions that are sampled by the interferometer.

3.1. Analytic Description for Power Law Distributions

The measured visibilities are given by the Fourier transform of the antenna weighted intensity distribution emergent from the globule. In our analysis, we must numerically model visibilities for comparison with the data. However, several simplifying assumptions exist that provide an analytic solution which affords some intuitive understanding of how the various physical quantities affect the visibilities.

For optically thin dust emission, the observed intensity at impact parameter b from a spherically symmetric globule is given by

$$I_\nu(b) = 2 \int_b^{R_{\text{out}}} B_\nu(T_d(r)) \kappa_\nu(r) \rho(r) \frac{r}{\sqrt{r^2 - b^2}} dr \quad (1)$$

where R_{out} is the outer radius of the globule, $T_d(r)$ the dust temperature, $\rho(r)$ the density, κ_ν the specific dust opacity, and $B_\nu(T)$ is the Planck function. If the density, and temperature follow simple radial power laws, $\rho \propto r^{-p}$, $T \propto r^{-q}$, and the opacity is a power law in frequency that does not vary along the line-of-sight, $\kappa_\nu \propto \nu^\beta$, then if the emission is assumed to be in the Rayleigh-Jeans (R-J) regime ($\hbar\nu/kT \ll 1$) from a globule with infinite outer boundary, the emergent intensity also has a simple power law form, i.e. $I(\nu, b) \propto \nu^{2+\beta} b^{-(p+q-1)}$ (Adams 1991). If we neglect the attenuation resulting from the antenna pattern of the interferometer, then the visibility distribution is also a power law, i.e. $V(\nu, u) \propto \nu^{2+\beta} u^{(p+q-3)}$, where u is the baseline length. With these approximations, the slope of the visibility profile — like the intensity profile — is determined solely by the sum of the power law indices assumed for the temperature and density. Note that a more steep density falloff with radius results in a less steep decrease in visibility with increasing baseline length. The relative brightness of the emission at different frequencies is determined by β , the dust opacity index.

3.2. Numerical Calculation of Model Visibilities

The synthetic visibility datasets used to compare with the observations are produced by a series of programs written in the Interactive Data Language (IDL) developed by Research Systems Inc.

The first step consists of simulating the emergent intensity distribution. Given inputs of model density and temperature distributions, and an adopted specific mass opacity, the program calculates the intensity image consisting of a 512×512 pixel array at resolution $0''.5$ per pixel, using the full Planck function for the emissivity, and integrates the radiative transfer equation through the model globule. These parameters determine the shape of the emergent intensity, and also the relative brightness at 1.2 mm and 3.0 mm (from the frequency dependence of the opacity). In general, each model is normalized by matching to the 1.3 mm flux measurement of Shirley et al. (2000), $F = 0.57 \pm 0.09$ Jy within a circular aperture (top-hat) of $40''$ diameter. The matching is achieved by iteratively scaling the product $\kappa_\nu \rho$ (κ_ν is the opacity, ρ the density). We adopt an outer boundary of $R_{\text{out}} = 0.15$ pc in the models; this is well constrained both by the extinction measurements (Harvey et al. 2001) and by molecular line observations (e.g. Zhou et al. 1990). Modifying the outer boundary assumption by as much as 50% was also found to have almost no discernable effect on our results.

The next step is to simulate observations of the model intensity images. The program approximates the antenna pattern of the IRAM dishes as a Gaussian of FWHM $50''$ ($100 \text{ GHz}/\nu$). Varying illumination, focus and pointing during the observations will cause the actual antenna pattern of the IRAM dishes to depart slightly from a pure Gaussian, but we expect this deviation to be small enough to have little impact on our analysis. We must account for the fact that the position of the peak millimeter emission is not exactly at the field center. To reduce the number of parameters to be fit, we fix the offset from the center as determined from a simple Gaussian fit to the 1.2 mm data: $\Delta\text{R.A.}$, $\Delta\text{Dec.} = (2''.23 \pm 0''.08, -0''.79 \pm 0''.12)$, giving coordinates for the peak of $\alpha = 19:37:00.89$, $\delta = 7:34:10.0$. Experimenting with offsets $\sim 0.1''$ different from these values showed no discernable change in the fitting results. The program performs an inverse FFT (to choose the positive sign in the exponential), and adjusts phase to take account of the offset position. This procedure results in an array of the visibility function sampled on a regular grid of u and v . The program then interpolates both the real and imaginary parts of the visibility to the exact (u, v) points sampled by the IRAM PdBI observations for comparison with the data.

3.3. Model Selections

As detailed above, the model visibilities are derived from the assumed (1) mass density distribution $\rho(r)$, (2) dust temperature distribution $T_d(r)$, and (3) specific mass opacity of the dust κ_ν . We consider the expected form of these quantities, and their uncertainties.

3.3.1. Density

The ultimate goal is to constrain the density distribution of B335, given realistic choices for the temperature and opacity. The most basic models are simple power laws with radius, with the aim to constrain the power law index p in the inner region. As an extension we also consider the physical models that arose in the Harvey et al. extinction study: (1) a Bonnor-Ebert sphere with $\xi_{max} = 12.5$, and (2) an inside-out collapse model with $R_{inf} = 0.03$ pc (25" at 250 pc). We also consider the effect of the bipolar outflow on the millimeter data, adopting the crude hollow cone description that successfully matched the near-infrared extinction data.

3.3.2. Temperature

For a optically thin dust envelope heated by a central source, the dust temperature distribution is expected to follow a power law with index determined by the frequency dependence of the opacity, i.e. $T_d(r) \propto L^{q/2}r^{-q}$, where $q = 2/(4 + \beta)$ (Doty & Leung 1994). Breakdowns in this approximation will occur at small radii where the envelope becomes optically thick to the bulk of the short wavelength emission (or there is a circumstellar disk), and at large radii where heating from the Interstellar Radiation Field (ISRF) becomes important.

For B335, the inner breakdown of the power law approximation is expected at radii $\lesssim 100$ AU, and would manifest as a steeply increasing temperature gradient. For the IRAM PdBI observations, the longest baseline of ~ 60 k λ corresponds to a linear resolution of ~ 900 AU. Hence, any optically thick region at small radii, or the presence of a disk, would appear as an unresolved component in these data. The nature and extent of the breakdown at large radii depends on the local strength of the ISRF. The modelling of Shirley et al. (2002) suggests that for typical envelope density distributions $\rho \propto r^{-p}$, with $p \sim 1-2$, the temperature follows very closely a power law description until falling to just under 10 K, where it flattens until at large radii external heating induces a rise to $\sim 12-15$ K. The detailed models of Shirley et al. (2002) for B335, using $p = 1.8$ and an opacity index $\beta = 1.8$, indicate that the temperature falls to about 10 K at a radius of ~ 5000 AU. For the model PdBI visibilities, any (small) variations in temperature beyond this radius have little effect

because the mass density has already decreased to $\sim 8 \times 10^4 \text{ cm}^{-3}$ (only 6% of its value at 1000 AU), and the interferometer begins to filter emission on angular scales much larger than the FWHM at 1.2 mm, $\sim 20''$ (~ 5000 AU). For our standard model, we adopt the simple power law, with a minimum temperature of 10 K, i.e.

$$T_d(r) = \begin{cases} 10 (5000 \text{ AU}/r)^{0.4} \text{ K} & \text{for } r \leq 5000 \text{ AU} \\ 10 \text{ K} & \text{for } r > 5000 \text{ AU} \end{cases} \quad (2)$$

In section 5.1.2 we investigate the uncertainties in the density profile that result from the temperature distribution in the model fitting process.

3.3.3. Mass Opacity

The mass opacity of dust grains in the millimeter region of the spectrum in protostellar envelopes is uncertain, but generally assumed to follow a power law with frequency, $\kappa_\nu \propto \nu^\beta$. The power law index varies depending on the dust properties, but tends to be bounded by a small range, roughly 1–2 (Ossenkopf & Henning 1994). For our standard model, we follow Looney, Mundy & Welch (2000) and adopt $\kappa_\nu = 0.1(\nu/1200 \text{ GHz}) \text{ cm}^2 \text{ g}^{-1}$, a power law with dust emissivity index β equal to unity. Since the globule is optically thin at the wavelengths of the PdBI observations, especially at 3.0 mm, the power law index in the models can be adjusted to produce the best simultaneous match at the two observed wavelengths.

4. Method for Fitting Model Parameters and Evaluating Fit Quality

The basic procedure is to maximize the probability distribution:

$$P(\text{Model} \mid \text{data}) = \prod_i e^{-(Z_i - f(x_i; p, m))^2 / 2\sigma_i^2} \times e^{-(m - m_0)^2 / 2\sigma_m^2} \quad (3)$$

where the Z_i are the visibility data points with uncertainty σ_i , $f(x_i; p, m)$ are the model data points, p a free parameter in the models, and m a model parameter about which we have a constraint (namely that it is a Gaussian random variable with mean m_0 and standard deviation σ_m). Maximizing the probability distribution is equivalent to minimizing the logarithm of its inverse. Taking account the fact that the Z_i are by nature complex visibilities, we want to minimize a modified χ^2 :

$$\tilde{\chi}^2 = \sum_i \frac{|Z_i - f(u, v; p, m)|^2}{\sigma_i^2} + \frac{(m - m_0)^2}{\sigma_m^2} \quad (4)$$

It is useful to be more explicit about the parameters p & m . The free parameter p is used to describe the shape of the model, e.g. the index of the power-law density distribution. The parameter m allows us to include observational uncertainties, e.g. the 20% uncertainty in the normalization of the model derived by matching the 1.3 mm flux measured by Shirley et al. (2000). This is achieved by allowing the 1.2 mm model visibilities to be scaled by a constrained parameter m , a Gaussian random variable with mean 1.0 and standard deviation 20%. For the 3.0 mm model visibilities, we use two different approaches: (1) scale the 3.0 mm data by the same factor m as the 1.2 mm data to force a dust opacity index of unity; (2) allow the 3.0 mm data to be freely scaled, to measure the dust opacity index and as a general check for consistency (by interpreting the derived value β in the context of the realistic range described above).

We select a model description and perform a fit for the model parameters by minimizing the modified χ^2 distribution which includes data at both wavelengths. Since the models are non-linear in the fitting parameters, we analyze the uncertainty in the best-fit model parameters using a Monte Carlo technique known as the *bootstrap* method (Press et al. 1992, p. 691). To describe this method, consider the dataset S used in the fitting. The first step is to construct a new dataset of equal size S' , by randomly selecting N times from the original dataset. This new sample is then analyzed in the same way as the original dataset, and the fitted model parameters recorded. This process is then repeated n times, where n is sufficiently large that the resulting distribution of best-fit model parameters is insensitive to its exact value (for our models, typically $n = 200$). If the fitting parameters may be successfully constrained by the data, then the distribution of best-fit parameters is very close to Gaussian, and the standard deviation of the distribution provides an estimate for the uncertainty of the parameters that best fit the original dataset.

The bootstrap method proves especially powerful for this analysis because small variations in the value of the modified χ^2 as defined above do not necessarily represent small variations in fit quality. The visibility dataset comprises a very large number of very low signal-to-noise measurements, which has the effect that the χ^2 wells are extremely shallow, and two models may seem almost equally good, despite the fact that there is ample signal to distinguish them. This occurs because the individual visibilities do not distinguish between the two models (represented in the χ^2 well being shallow) but the combination of all the individual visibilities does (represented by a lower χ^2 corresponding to a better fit). This issue could be circumvented by binning the visibilities e.g. radially, to increase the signal-to-noise, and then performing a χ^2 fit to the binned values. We avoid this solution because the binning loses information on the asymmetry of the globule that is hidden in the dataset by the vectorial nature of visibility data. For the spherically symmetric models, we bin the data for graphical comparison with the models.

The shallowness of the χ^2 wells results in the minimum values of the reduced χ^2 for various models to all have similar absolute values, in the range $\chi_\nu^2 = 1.4\text{--}1.5$. While a lower value of χ_ν^2 may be interpreted as providing a better fit, the small range of variation confuses the differences in the fit quality. Therefore, we adopt graphical techniques to express the superiority of one model fit over another.

5. Results and Analysis

Table 1 summarizes the results from the χ^2 fits to several spherically symmetric models, as well as axisymmetric models. For fits marked ‘#a’, the normalization of the 3.0 mm visibilities is constrained by fixing the dust opacity index β to unity. For fits marked ‘#b’, the dust opacity index is included as an additional fitting parameter.

5.1. Spherically Symmetric Models (Fits I–IV)

Although the B335 dense core shows clear departures from spherical symmetry when viewed both in dust extinction and molecular emission, for simplicity and insight we start by investigating spherically symmetric density models. In Fits Ia & Ib, we use a power law model for the density distribution. In Fit IIa, we use a power law density model but include an additional point source component to the intensity distribution. We also consider Bonnor-Ebert spheres (Fit IIIa; Bonnor 1956, Ebert 1955), and the Shu (1977) inside-out collapse model (Fit IVa).

5.1.1. Single Power Laws

In the simplest model, the density distribution is described by a single power law. The best-fitting model has a power law index of $p = 1.65 \pm 0.05$ (Fit Ib) with a dust opacity index $\beta = 0.81 \pm 0.12$ that is consistent with unity. Fit Ia, which assumes $\beta = 1$, gives a density power law index that agrees within uncertainties with that for Fit Ib. Figure 1 shows a plot of binned visibility amplitude vs. (u, v) distance for both wavelengths. The binning is logarithmic and oversamples the data by a factor of 2; filled symbols and non-filled symbols are not completely independent. The amplitudes are the vectorial mean of the complex visibilities in each bin (corrected for the offset phase center), the error bars represent one standard deviation in the mean. For the dust emission at both wavelengths, the decrease in visibility amplitude with baseline length may be well described by a power law. The plots

also show the visibility curves for the best fit model ($p = 1.65$) and models that deviate by $\pm 2\sigma$ ($p = 1.55$ and $p = 1.75$). These models have not been scaled by the fitting parameters since this term contributes to the χ^2 and its exclusion allows the differing quality of each fit to be better seen (note that the $\pm 2\sigma$ models require a scaling at 1.2 mm of 1.19 and 0.75 for $p = 1.55$ and $p = 1.75$, respectively).

5.1.2. *Sensitivity to Temperature Assumptions*

These results use the temperature distribution described in section 3.3.2, which is based on a physical argument. To understand the sensitivity of the density power law results to the temperature, we investigate how subtle quantitative changes affect the results by repeating the fitting procedure with temperature distributions that (1) have different (constant) temperature in the outer envelope, and (2) have different power law indices.

We find that the fitted density power law index is insensitive to (small) changes in the envelope temperature: variations of ± 2 K lead to variations in the inferred density slope of much less than the quoted uncertainty. The main reason is that the antenna FWHM is only $20''$ at 1.2 mm (which has the higher signal-to-noise ratio of the two wavelengths), and the data are not very sensitive to the temperature structure at larger radii. Therefore, uncertainties in the strength of the ISRF are relatively unimportant in this study.

Changes in the power law index of the inner temperature distribution produce more significant changes in the fitting results. The globule envelope is optically thin at both wavelengths; if the R-J approximation were also to hold, then the inferred density power law index p would be related to the temperature power law index q by the relation $p + q = \text{constant}$. However, the R-J approximation breaks down, especially at 1.2 mm, with the consequence that p is more sensitive to changes in q . We find that varying q by ± 0.1 leads to variations in p at the level of $\simeq \mp 0.15$.

5.1.3. *Sensitivity to an Unresolved Central Component*

As already noted, there may exist a central region of B335 for which the envelope will be optically thick at infrared wavelengths, causing the temperature profile to depart from a simple power law. In this region, the temperature is expected to climb very sharply with radius, resulting in increased emission at long baselines beyond the extrapolation of a simple power law. The presence of an unresolved disk, effectively a warm central point source, would have a similar effect. While the PdBI data samples insufficient baseline lengths to directly

measure the flux of any such compact component, it will, if present, flatten the visibility profiles of the various models and therefore affect the fitted density power law index. Fit IIa quantifies the effect using the combination of the simple power law for density, temperature and mass opacity from Fit Ia, but including an additional point source component with $F \propto \nu^3$ (i.e. the spectrum of a source where the majority of the emission is optically thin at 1.2 mm, with a dust opacity index of unity). For a point source flux $F = 12 \pm 7$ mJy at 1.2 mm, the most allowed by the measurements at long baselines, the fitted density index is reduced to $p = 1.47 \pm 0.07$. This point source flux corresponds to an implied disk mass of $M \simeq 2 \times 10^{-3} M_{\odot}$ ($60 K/T_{\text{disk}}$) for our adopted opacity law. This is at the lower end of the 0.002 – $0.3 M_{\odot}$ range of disk masses that have been observed around T Tauri stars by Beckwith et al. 1990. Since accretion disks result from conservation of angular momentum during the collapse process, the small inferred mass of the disk may be related to the fact that B335 has a relatively low rotation rate (Frerking, Langer & Wilson 1987). However, accretion disks may also be connected with the driving source of bipolar outflows, and the B335 outflow is not unusual, with size, momentum and energy typical for a low mass protostar (Goldsmith et al. 1984).

When a compact source of emission is included in the analysis, the fitted density power law index is reduced by ~ -0.2 . Thus, possible point source “contamination” is the dominant source of systematic uncertainty in the fitted density structure. This is also the case in single dish measurements, where a point source can add a systematic uncertainty of up to ~ -0.5 to the inferred density index (e.g. Shirley et al. 2002).

Table 2 summarizes various sources of systematic error and the level of uncertainty that the variations contribute to the fitted density power law index in the spherically symmetric models.

5.1.4. Comparison With Previous Studies

The best fit density power law index of $p = 1.65$ is slightly less steep than the value of $p = 1.8$ found by Shirley et al. (2002) from SCUBA data. It is perhaps significant that the results from the two instruments are consistent to within the uncertainties considering the resolution of the JCMT at $850 \mu\text{m}$ is $15''$, roughly encompassing the entire range of radii probed by the the IRAM PdBI. However, even taking account all sources of uncertainty, the best-fit power law index of $p = 1.65$ is significantly less steep than the $p = 2.0$ power law index of the hydrostatic isothermal sphere that so successfully matches the outer envelope of B335 in near-infrared extinction (Harvey et al. 2001) and dust emission shape (Shirley et al. 2002) This result suggests that the density profile becomes less steep in the inner regions

($r \lesssim 25''$), a conclusion also suggested by the extinction data, where two models with this character (inside-out collapse and the Bonnor-Ebert sphere) provided better fits than a single power law.

5.1.5. *Broken Power Laws, Inside-Out Collapse, Bonner-Ebert Sphere*

We have also investigated models with density distributions that flatten in the inner region: (1) a broken power law, with fixed index of $p = 2$ in the envelope, with model parameters the break radius and inner power law index; (2) an inside-out collapse model with model parameter the infall radius (this is approximately a special case of the broken power law); and (3) a Bonnor-Ebert sphere, where the model parameter is the dimensionless outer radius of the sphere ξ_{\max} . None of these models fit the data nearly as well as a single power law.

For the broken power law model, it proved impossible to obtain robust results for the two fitted parameters, which are coupled and have comparable effects in the simulated datasets. Decreasing the break radius, or increasing the power law index in the inner region; each steepens the apparent density profile, and it is not possible to distinguish between the two effects.

The inside-out collapse model and the Bonnor-Ebert sphere that matched the extinction data both provide poor fits to the visibility data that sample the envelope closer to the protostar. Figure 2 shows a comparison between the binned visibility amplitude vs. (u, v) distance and the curves produced from these models: the inside-out collapse model with $R_{\inf} = 0.03$ pc, and the Bonnor-Ebert sphere with $\xi_{\max} = 12.5$. There are large discrepancies between these models and the data. Because these models so poorly describe the data, the χ^2 statistic provides a poor discriminant of model parameters. At the χ^2 distribution minimum, the bootstrap calculation bounces between the end points of the grid at each iteration, no matter how wide a range of model parameters are considered. Essentially, the data prefer a model with a single power law index $p \simeq 1.65$, and neither the inside-out collapse model nor the Bonner-Ebert sphere model can produce an equivalent slope over a sufficiently large enough range in spatial scales.

The inclusion of a point source component does not rectify the problems in fitting with these two physical models, despite effectively reducing the slope of the fitted density distribution. The Bonner-Ebert sphere has a relatively flat density distribution at small radii, and therefore the visibilities drop sharply at long baselines. Adding a point source to the Bonnor-Ebert sphere model adds intensity at long baselines but still cannot produce

a good fit over the large range in spatial scale sampled by the data. For the inside-out collapse model, the fit fails to constrain the infall radius because this parameter does not affect the slope of the density distribution in the region where the data provide constraints (e.g. $R_{\text{inf}} \gtrsim 0.024$ pc = $20''$ at 250 pc).

A combination of the inside-out collapse model with a point source also produces a poorer fit to the data than does a simple power law with a point source. The χ^2 of this model is equivalent to power laws that are nearly 3σ away from the best fit (i.e. the fit quality is equivalent to the power law models with $p = 1.30$ or $p = 1.65$, when the best fit is for $p = 1.47 \pm 0.07$). This seems a surprising result, since the standard impression of the inside-out collapse model is that it behaves like a power law with index very close to 1.5 in the infalling region. But, while this is asymptotically true at very small radii, the local power law index of the inside-out collapse solution in fact decreases as one moves outwards in the infalling region, attaining a minimal value close to unity just within the infall radius. This means that for the same total flux within a $40''$ diameter, the inside-out model has greater intensity at larger radii than does a simple $p = 1.5$ power law. The effect is that while the slopes of the two visibility profiles are similar in the spatial range where the PdBI data are sensitive, the primary beam attenuation (FWHM $\simeq 20''$ at 1.2 mm) causes the inside-out model visibilities to be 25% fainter than the single power law model. The required increase in the scaling parameter, m , to best match the data is significant and contributes to the increased value of χ^2 , resulting in a worse fit for the inside-out collapse model. Essentially, the inside-out collapse model cannot simultaneously match the Shirley et al. (2000) flux measurement and the normalization of our observed visibility profile.

5.2. Axisymmetric Models (Fit V)

In Figure 3, left column of panels show images of B335 made from the 1.2 mm and 3 mm visibilities, respectively. These images show that the B335 dense core is not spherically symmetric at this size scale, but rather is more like an oblate spheroid, flattened along the axis of the bipolar outflow (nearly East-West on the sky). In Figure 3, the second column of panels shows images of the best fit spherically symmetric models, made by processing the synthetic visibilities in the same way as the data. The aspect ratio of the emission is clearly different between the models and the data. The asymmetry may be caused by the action of the outflow, or it may reflect a flattening in the initial configuration of the core.

For the dust extinction data at scales $\gtrsim 3500$ AU, the asymmetry was well reproduced by a model that assumed that the outflow had hollowed out a bipolar cone, with best fit constant semi-opening angle $\alpha = 41^\circ \pm 4^\circ$. To extend the analysis of the visibility data,

we have added the same simple representation of the bipolar outflow to the power law density distribution models to determine if this model can also successfully explain the asymmetry in the observed dust emission. In these models, we assume no unresolved point source of significant flux, having already quantified the effect of this additional component in section 5.1.3. We also assume that the temperature remains a simple radial power law. This is an extreme simplification as the emptied outflow cavities provide a less obscured view to the hotter inner region, and as a result the temperature of dust near to the boundary of the outflow cavity will likely have been underestimated.

Fit V (a & b) repeats the recipe of the χ^2 analysis, using a density model that comprises a radial power law with index p and a hollow-cone outflow with constant semi-opening angle α . As with Fit Ia, Fit Va assumes a dust opacity index of unity, whereas Fit Vb includes the dust opacity index as an additional parameter. As listed in Table 1, the two fits give nearly identical results, both with each other and with the outcome of Fit I. The best fit power law index (Fit Vb) is $p = 1.65 \pm 0.05$, with outflow semi-opening angle $\alpha = 40^\circ \pm 5^\circ$, and dust opacity index $\beta = 0.74 \pm 0.10$.

In Figure 2, the additional columns of panels show images at both wavelengths made from the synthetic visibilities of the best fit model, and those with parameter values that differ by 2σ from the best fit, i.e. $p = 1.55$, $\alpha = 30^\circ$ and $p = 1.75$, $\alpha = 50^\circ$. The best fit spherically symmetric model is also shown to demonstrate the effect of adding the outflow cones. The quality of the match to the data is visible in (1) the extent of the apparent asymmetry, and (2) the number and spacing of the intensity contours. Note that the density gradient parameterized by p and the degree of asymmetry parameterized by α are nearly independent. The outflow model with $p = 1.65$ and $\alpha = 40^\circ$ provides the best match to the imaged data, and has lower reduced χ^2 despite the additional fitting parameter.

The best fit density power law index is essentially unchanged from the spherically symmetric analysis. That these results should be so similar is partly a consequence of the adopted outflow geometry. The main effect of the outflow cone is to change the normalization of the intensity profile along the direction through the cone, but not to change the shape or power law index of the profile. This would not be the case for an outflow model without a constant opening angle. For instance, for a model where the opening angle decreases with distance from the protostar (e.g. a parabola), the intensity profile along the outflow axis becomes less steep as relatively less material is removed from the core at larger radii. The fitted power law index in such a model would be higher than for the simple cone model. As an example, consider an outflow geometry where the semi-opening angle is 50° at 500 AU, decreasing to 30° at 5000 AU; in this model, the intensity profile along the outflow axis has power law index that is ~ 0.15 less steep than for the constant opening angle case, or the profile

along an axis perpendicular to the flow. While we have not analyzed this class of model in detail, since the outflow covers less than two quadrants of the sky, spatial averaging of the regions affected by the outflow and the regions that are unaffected suggests an uncertainty of roughly $\delta p \lesssim 0.15/2 \sim 0.08$, a small effect on fitted power laws.

The good agreement in the fitted opening angles for the simple cone model in this work and the extinction study of Harvey et al. (2001) may not be especially significant. While the consistency is encouraging, it most likely reflects the fact that the crude outflow model creates a detectable degree of oblate flattening only for semi-opening angles near 45° . For much larger opening angles, too much of the dense core is removed by the outflow and the core becomes disk like; for much smaller angles, the effect on the core is small, except in a small region at the poles.

5.3. Discussion

The analysis presented in the previous sections provides strong evidence that the density distribution power law index is less than 2.0 in the central 5000 AU ($20''$) region where the PdBI observations are sensitive. The best fit single power law for the density distribution has index of $p = 1.65 \pm 0.05$. This value should be considered an upper limit since including a central point source — the dominant contributor of systematic uncertainty — can reduce the value to $p = 1.47 \pm 0.07$. The remaining sources of systematic uncertainty considered, of which the most important is the radial dependence of the temperature distribution, likely contribute a total uncertainty at the level $\delta p \lesssim 0.2$.

The Harvey et al. (2001) extinction study demonstrated a density index of very close to 2.0 ($p = 1.91 \pm 0.07$) over a 3500–25000 AU range in radius, indicative of an isothermal hydrostatic envelope, a result consistent with several different analyses of dust emission from single dish observations that probe similar spatial scales (Shirley et al. 2002, Motte & André 2001). The new interferometric dust emission data, which probes smaller scales, provides strong evidence that the density profile becomes less steep in the inner 5000 AU of B335. This conclusion agrees with the hints from detailed modelling of dust extinction indicative of a turnover in the density profile at a radius of about 6500 AU, as well as application of the Shu (1977) inside-out collapse model to molecular line observations (Zhou et al. 1993, Choi et al. 1995).

The inferred density profile of the B335 core conforms closely to the predictions in standard theories of isolated star formation (Shu 1977, Larson 1969, Penston, 1969) where an envelope with density power law index of $p = 2.0$ surrounds an inner region with a $p = 1.5$

distribution characteristic of material freely falling under the force of gravity. However, even with the contribution of a unresolved point source component, the specific Shu (1977) inside-out collapse model provides a worse fit to the data than does a simple power law. The local density index within the turnover (infall) radius in the inside-out collapse model is significantly less steep than $p = 1.5$, ranging from roughly unity to 1.5. Consequently, the inside-out collapse model cannot successfully match both the normalization of the visibility profile in the IRAM PdBI observations and the total flux within a large aperture measured with a single dish by Shirley et al. (2000). The constraint provided by the single dish measurement — effectively the visibility information at zero-spacing that cannot be measured directly by the interferometer — is crucial to this analysis; without it, the density distribution power law index can be constrained only to within $\delta p \sim \pm 0.3$, not including contributions from systematic errors.

The images of B335 presented in Figure 3 demonstrate clear departures from spherical symmetry. The inner part of the globule appears significantly extended perpendicular to the outflow axis. This is in contrast to images of dust emission with lower angular resolution that show nearly spherical symmetry. While there are no robust predictions for the effect of the outflow on the density distribution, combining the power law density model with a very simple bipolar cone to describe the outflow improves the match to the data, but does not alter significantly the inferred shape of the radial variation in density.

Observations of B335 at longer baselines are needed to constrain the flux from any point source component that may be present at the center of the dense core. Such a component might be expected in the form of a circumstellar disk. Indeed, the maximal 1.2 mm flux of an unresolved component (~ 12 mJy) lies on the low end of the range expected for the B335 disk based on the subarcsecond submillimeter fluxes for Class 0 sources observed with the CSO-JCMT interferometer (Brown et al. 2000), perhaps related to the relatively low rotation rate of B335 (see Zhou 1995).

In the future, high resolution observations of B335 at submillimeter wavelengths may help to mitigate the uncertainties associated with the temperature distribution. Spatial information on the optically thin emission distribution at a third wavelength that is sufficiently short to be outside the Rayleigh-Jeans regime for the majority of the dense core should allow for partly breaking the degeneracy between temperature, density and opacity. Such observations may be obtained with the Submillimeter Array (SMA), now under construction, or the Atacama Large Millimeter Array (ALMA).

5.4. A Physical Density Distribution for B335

Throughout the analysis presented so far, attention has been paid only to the power law index of the density distribution; the normalization has been absorbed in satisfying the constraint placed by the single dish 1.3 mm flux measurement of Shirley et al. (2000). To allow the results to be used in future modeling of B335, we now discuss the physical scale of the density distribution. The present study, in concert with the Harvey et al. (2001) extinction work, affords the unique position to propose a density distribution that satisfies both dust emission and extinction data over a range in radius from 500 AU to 25,000 AU.

For the adopted temperature distribution and mass opacity at 1.2 mm, the density within $r \lesssim 20''$ (5000 AU) is:

$$n_H(r) \simeq \begin{cases} 8.1 \times 10^5 \text{ cm}^{-3} \left(\frac{r}{10^3 \text{ AU}} \right)^{-1.65} & \text{for no point source} \\ 7.6 \times 10^5 \text{ cm}^{-3} \left(\frac{r}{10^3 \text{ AU}} \right)^{-1.47} & \text{for 12 mJy point source} \end{cases} \quad (5)$$

where n represents the total number density in the gas ($n = n(H_2) + n(He) + \dots = \rho/(\mu m_H)$, $\mu = 2.29$). Note that including the outflow as a hollow cone with semi-opening angle 40° increases by 14% the coefficient of the density distribution power law (and leaves the index unchanged).

For the envelope beyond $r \gtrsim 26''$ (6500 AU), the Harvey et al. (2001) extinction work suggested an isothermal, hydrostatic, structure with r^{-2} , consistent with the results of the dust emission studies of Shirley et al. (2002) and Motte & André (2001). This envelope density distribution can be adopted into our model without affecting the inferred structure in the inner regions, since emission from the envelope is a negligible contribution at small impact parameters ($\lesssim 20''$), and is filtered out at large impact parameters by the antenna pattern (20'' FWHM at 1.2 mm). However, the correct normalization of the density distribution in the outer envelope relative to the inner regions is difficult to assess because the uncertainties involved in the extinction work (gas-to-dust ratio, reddening law) are different from those that arise in the dust emission studies (specific mass opacity, temperature structure), and the previous dust emission studies do not resolve the inner regions.

The analysis of the interferometer dust continuum data allows us to draw some conclusions about the behaviour of the density profile in the transition region between the two regimes, and hence to infer a consistent scale for the envelope. In order for any model to simultaneously match the normalization of the observed visibility profile and the Shirley et al. (2000) measurement of the flux within $r < 20''$, the local power law index in the transition region cannot decrease from the value measured in the inner region. The power law index must remain constant or become steeper. A simple continuation of the inner power law until

reaching the envelope implies a density distribution for $r > 26''$ (6500 AU):

$$n(r) \simeq \begin{cases} 1.6 \times 10^4 \text{ cm}^{-3} \left(\frac{r}{10^4 \text{ AU}}\right)^{-2.0} & \text{for no point source} \\ 2.2 \times 10^4 \text{ cm}^{-3} \left(\frac{r}{10^4 \text{ AU}}\right)^{-2.0} & \text{for 12 mJy point source} \end{cases} \quad (6)$$

For the case of no point source, this composite density distribution gives an average power law index of $p = 1.90$ over the 3500–25000 AU radius range sampled by the dust extinction data, precisely reproducing the extinction result ($p = 1.91 \pm 0.07$), and it gives an average power law index of $p = 1.80$ over the 1000–25000 AU radius range, which reproduces the result of Shirley et al. (2002). Remarkably, the normalization of this envelope distribution is also within 6% of the singular isothermal sphere.

6. Summary

We present a study of the density distribution of the protostellar collapse candidate B335 using continuum observations at 1.2 mm and 3.0 mm made with the IRAM PdBI. In summary:

1. We perform a detailed analysis of the interferometer measurements directly in the visibility domain, not in the image domain. Though computationally intensive, this approach avoids the limitations of standard Fourier inversion and deconvolution algorithms.
2. The PdBI visibility data strongly constrain the density distribution at radii from ~ 500 AU to ~ 5000 AU from the protostar. Within this inner region, the density distribution is well described by a single power law. The best fit power law index $p = 1.65 \pm 0.05$ (1σ) is significantly less steep than values close to $p = 2.0$ derived for larger radii from analyses of dust emission and extinction. We consider the effects of various sources of systematic uncertainty on the derived value of p . Including a central source of point-like emission in the model, as might come from an unresolved accretion disk, reduces the power law index to $p = 1.47 \pm 0.07$. The remaining sources of systematic uncertainty, of which the most important is the radial dependence of the temperature distribution, likely contribute a total uncertainty at the level of $\delta p \lesssim 0.2$.
3. The inferred density profile for B335, with a power law index close to $r^{-1.5}$ near the protostar within an r^{-2} envelope, matches the generic paradigm of gravitational collapse for isolated, low mass star formation. However, the specific inside-out collapse solution of Shu (1977) does not produce as good a fit to the dust emission data in the

inner region as does a simple single power law, largely because of the shallow slope ($p \sim 1$) of the inside-out collapse solution just within the infall radius.

4. Images made from the visibility data show clear departures from spherical symmetry, with the inner part of the B335 core elongated perpendicular to the outflow axis. Including the outflow in the model fitting as a hollowed bipolar cone improves the match to the data and does not significantly change the derived radial density power law index from the value obtained in the spherically symmetric analysis. An outflow geometry where the opening angle decreases with distance from the protostar location would result in a slightly larger power law index, roughly $\delta p \lesssim 0.05$.
5. Observations that probe the subarcsecond millimeter continuum structure of B335 are needed to constrain the central point source contribution to the dust emission.

DWAH thanks Jonathan Jenkins for many useful discussions concerning statistics. We acknowledge the IRAM staff from the Plateau de Bure and from Grenoble for carrying out the observations and for their help during the data reduction. We are especially grateful to Roberto Neri for his assistance. Partial support for this work was provided by NASA Origins of Solar Systems Program Grant NAG5-6266.

REFERENCES

Adams, F.C. 1991, *ApJ*, 382, 544

Beckwith, S.V.W., Sargent, A.J., Chini, R.S. & Güsten, R. 1990, *AJ*, 99, 924

Bonnor, W. 1956, *MNRAS*, 116, 351

Brown, D.W., Chandler, C.J., Carlstrom, J.E., Hills, R.E., Lay, O.P., Matthews, B.C., Richer, J.S. & Wilson, C.D. 2000, *MNRAS*, 319, 154

Caselli, P., Walmsley, C.M., Zucconi, A., Tafalla, M., Dore, L. & Myers, P.C. 2002, *ApJ*, 565, 331

Chandler, C.J. & Sargent, A.L. 1993, *ApJ*, 414, 29

Choi, M., Evans, N.J.II, Gregerson, E.M., Wang, Y. 1995, *ApJ*, 448, 742

Doty, S.D. & Leung, C.M. 1994, *ApJ*, 424, 729

Ebert, R. 1955, *Z.Astrophys.*, 37, 217

Frerking, M.A., Langer, W.D. & Wilson, R.W. 1987, *ApJ*, 313, 320

Goldsmith, P.F., Snell, R.L., Hemeon-Heyer, M. & Langer, W.D. 1984, *ApJ*, 286, 599

Harvey, D.W.A., Wilner, D.J., Lada, C.J., Myers, P.C., Alves, J.F. & Chen, H. 2001, *ApJ*, 563, 903

Hirano, N., Kameya, O., Kasuga, T. & Umemoto, T. 1992, *ApJ*, 390, 85

Hogerheijde, M.R., van Dishoeck, E.F., Salverda, J.M. & Blake, G.A. 1999, *ApJ*, 513, 350

Keene, J., Davidson, J.A., Harper, D.A., Hildebrand, R.H., Jaffe, D.T., Loewenstein, R.F., Low, F.J. & Pernic, R. 1983, *ApJ*, 274, 43

Keene, J. & Masson, C.R. 1990, *ApJ*, 355, 635

Larson, R.B. 1969, *MNRAS*, 145, 271

Looney, L.W., Mundy, L.G. & Welch W.J. 2000, *ApJ*, 529, 477

Motte, F. & André, P. 2001, *A&A*, 365, 440

Mundy, L.G., Looney, L.W. & Welch W.J. 2000, in *Protostars and Planets IV*, eds. V. Mannings, A.P. Boss and S.S. Russell, (Tucson: University of Arizona Press), p. 355

Ossenkopf, V. & Henning, T. 1994, *A&A*, 291, 943

Penston, M.V. 1969, *MNRAS*, 144, 425

Press, W.H., Teukolsky, S.A., Vetterling, W.T. & Flannery, B.P. 1992, *Numerical Recipies in C*, p. 691

Saito, M., Sunada, K., Kawabe, R., Kitamura, Y. & Hirano, N. 1999, *ApJ*, 518, 334

Shirley, Y.L., Evans, N.J.II & Rawlings, J.M.C. 2002, *Astro-Ph*, 0204024

Shirley, Y.L., Evans, N.J.II, Rawlings, J.M.C. & Gregerson, E.M. 2000, *ApJS*, 131, 249

Shu, F.H. 1977, *ApJ*, 214, 488

Tafalla, M., Myers, P.C., Caselli, P., Walmsley, C.M. & Comito, C. 2002, *ApJ*, 569, 815

Tomita, Y., Saito, T. & Ohtani, H. 1979, *PASJ*, 31, 407

Visser, A.E., Richer, J.S. & Chandler, C.J. 2001, *MNRAS*, 323, 257

Ward-Thompson, D., Scott, P.F., Hills, R.E. & Andre, P. 1994, *MNRAS*, 268, 276

Ward-Thompson, D., Motte, F. & André, P. 1999, *MNRAS*, 305, 143

Wilner, D.J., Myers, P.C., Mardones, D. & Tafalla, M. 2000, *ApJ*, 544, 69

Zhou, S., Evans, N.J.II, Butner, H.M., Kutner, M.L., Leung, C.M. & Mundy, L.G. 1990, *ApJ*, 363, 168

Zhou, S., Evans, N.J.II, Kompe, C. & Walmsley, C.M. 1993, *ApJ*, 404, 232

Zhou, S. 1995, *ApJ*, 442, 685

Table 1. Summary of the Density Model Fits

Fit	Density Model	Dust Index	Fitted Model Parameter(s)	χ^2_ν
Ia	Power law: $\rho \propto r^{-p}$	$\beta = 1$	$p = 1.61 \pm 0.06; M = 1.10 \pm 0.13$	1.4647
Ib	As Fit Ia	$\beta = \text{Free}$	$p = 1.65 \pm 0.05; \beta = 0.81 \pm 0.12$	1.4646
IIa	Power law + point flux F	$\beta = 1$	$p = 1.47 \pm 0.07; F = 12 \pm 7 \text{ mJy}; M = 1.24 \pm 0.15$	1.4645
IIIa	Bonner-Ebert, $\xi_{\max} = 12.5$	$\beta = 1$...	1.5025
IVa	Inside-out, $R_{\text{inf}} = 0.03 \text{ pc}$	$\beta = 1$...	1.4674
Va	Power law + outflow	$\beta = 1$	$p = 1.60 \pm 0.06; \alpha = 38^\circ \pm 5^\circ; M = 1.10 \pm 0.13$	1.4625
Vb	As Fit Va	$\beta = \text{Free}$	$p = 1.65 \pm 0.05; \alpha = 40^\circ \pm 5^\circ; \beta = 0.74 \pm 0.10$	1.4622

Table 2. Summary of systematic uncertainties in the fitted density power-law index p

Model Parameter	Variation	Resulting δp Systematic Error
Temperature power-law index, q	$\delta q \lesssim \pm 0.1$	$\lesssim \mp 0.15$
Outer envelope temperature (ISRF)	$\delta T \lesssim \pm 2$ K	$\lesssim \pm 0.05$
Central point source, flux F	$F = 12 \pm 7$ mJy	-0.18 ∓ 0.1
Dust opacity spectral index β	$\beta = 1 \rightarrow \beta = \text{free}$	$\simeq 0.05$
Outer boundary of B335, R_{out}	$\delta R_{\text{out}}/R_{\text{out}} \lesssim 50\%$	$\lesssim 0.01$
Outflow cone geometry, $\alpha = \alpha(r)$	$\delta \alpha(r) \lesssim \pm 20^{\circ}$ ¹	$\lesssim \mp 0.08$

¹Refers to an outflow geometry where the opening angle changes monotonically by 20° over the 500–5000 AU range in radius to which the data is sensitive.

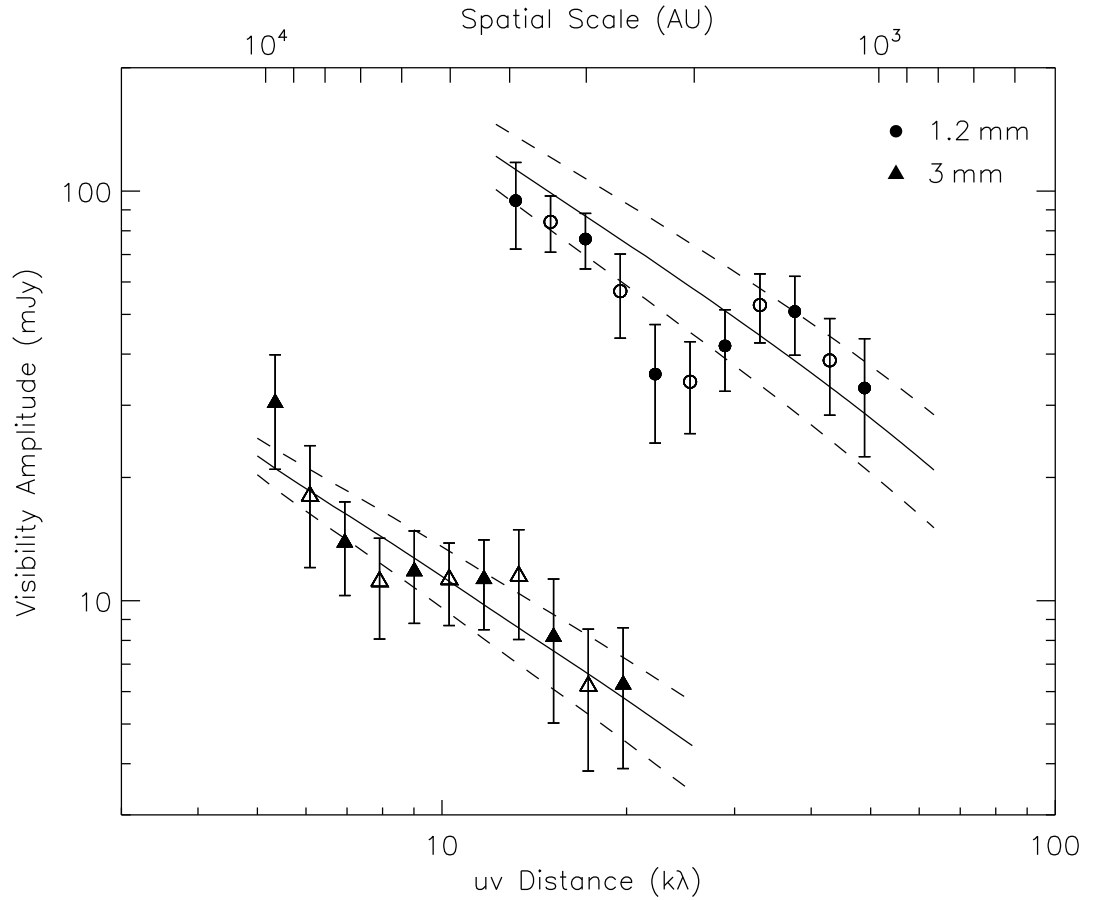


Fig. 1.— Binned visibility amplitudes against (u, v) distance at 3.0 mm (triangles) and 1.2 mm (circles) for the PdBI observations of B335 together with the unscaled curves for the best fitting single power law model $p = 1.65$ (solid line), and power law models that deviate by 2σ , $p = 1.55$ (lower dashed line) and $p = 1.75$ (upper dashed line). Note that the bins oversample the data and the filled symbols are not completely independent from non-filled symbols. The spatial scale on the top is defined as $250 \text{ pc} \times \lambda/D$, where D is the baseline length.

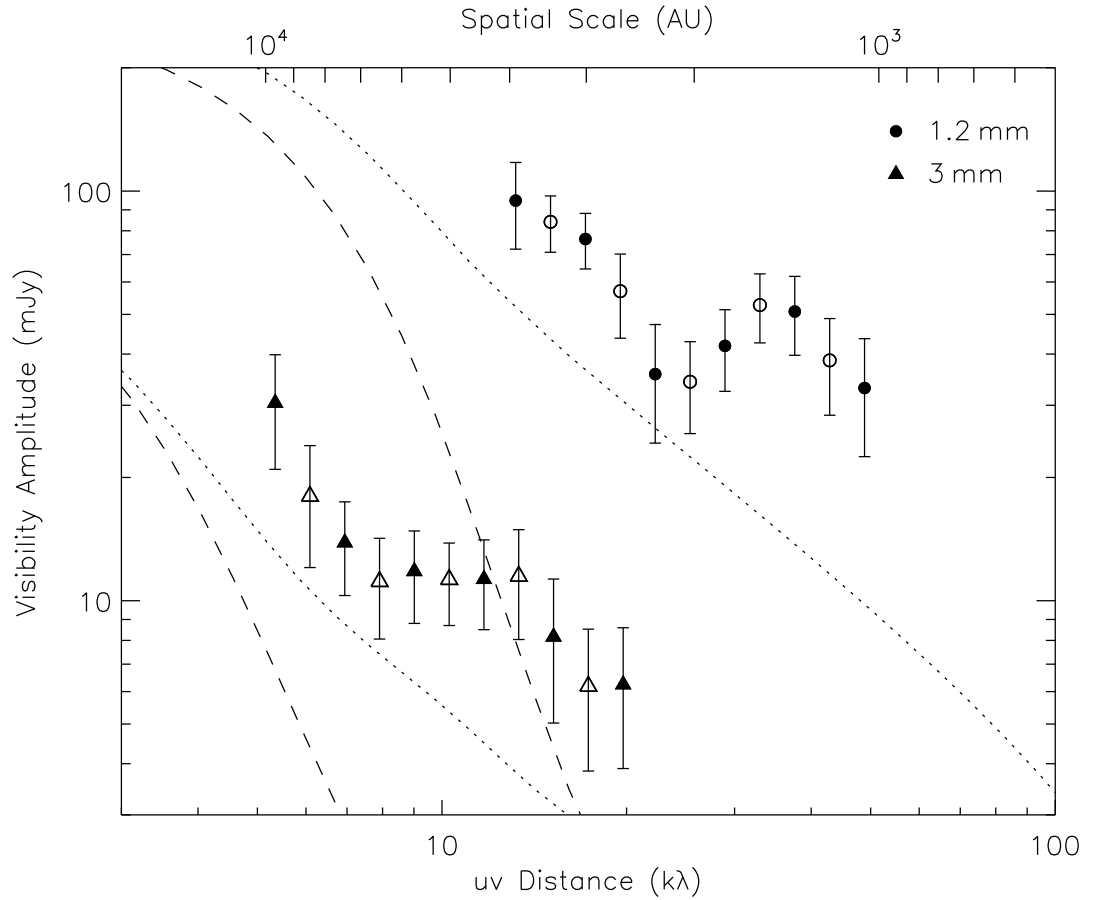


Fig. 2.— Binned visibility amplitudes against (u, v) distance at 3.0 mm (triangles) and 1.2 mm (circles) for the PdBI observations of B335 together with theoretical curves for the Bonnor-Ebert sphere with $\xi_{\max} = 12.5$ (dashed line) and the inside-out collapse model with $R_{\inf} = 0.03$ pc (dotted line). Neither of these models can successfully match the data. The bins oversample the data and the filled symbols are not completely independent from non-filled symbols. The spatial scale on the top is defined as $250 \text{ pc} \times \lambda/D$, where D is the baseline length.

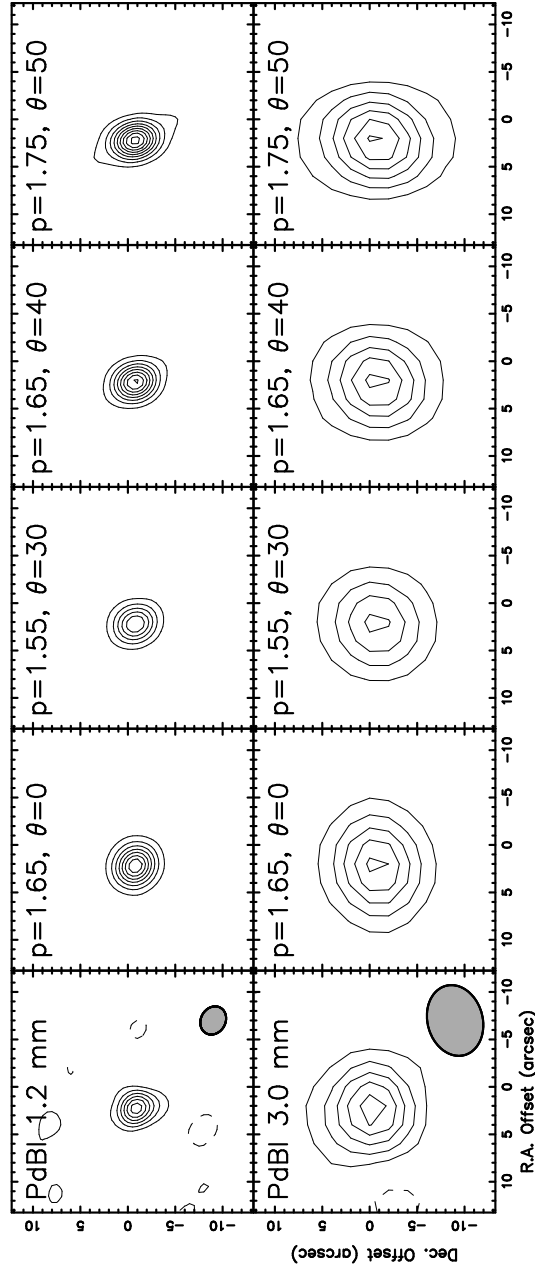


Fig. 3.— Images of B335 at 1.2 mm (top panels) and at 3.0 mm (lower panels). The left column shows images made from the PdBI data, and the columns to the right show images made from synthetic datasets produced from the various protostellar envelope models, including the best fit spherically symmetric power law model, $p = 1.65$, and the best-fit asymmetric model, $p = 1.65$, $\alpha = 40^\circ$, bracketed by asymmetric models with parameter values that differ by 2σ , i.e. $p = 1.55$ and $\alpha = 30^\circ$, $p = 1.75$ and $\alpha = 50^\circ$. The contour levels are $(2, 4, 6, 8, \dots) \times$ the rms noise of the imaged data at each wavelength, 3.0 mJy for the 1.2 mm panels and 0.8 mJy for the 3.0 mm panels. The synthesized beam sizes are shown in the lower right corners of the imaged data in the first column.